nature communications

Article

https://doi.org/10.1038/s41467-025-65430-7

Spin transition in magnesiowüstite and ultralow thermal conduction in ultralow velocity zones

Received: 31 March 2025

Accepted: 15 October 2025

Published online: 25 November 2025

Check for updates

Wen-Pin Hsieh[1,2] ✉, Frédéric Deschamps[1], Yi-Chi Tsao[1], Allison Pease[3], Susannah M. Dorfman[3], Hannah J. Bausch[4] & Fei Wang[5]

Above Earth's core-mantle boundary (CMB), seismic studies revealed numerous enigmatic, small-sized patches of ultralow velocity zones (ULVZs) with anomalously lower velocities and higher density than ambient mantle. These regions may be enriched in Fe-rich oxides, and their thermal conductivity Λ would critically influence regional heat-flux and thermochemical evolution around CMB, but remains poorly constrained. Here we experimentally show that Λ of $(Mg_{0.75},Fe_{0.25})O$, Λ_{Fp25}, and $(Mg_{0.25},Fe_{0.75})O$, Λ_{Fp75}, both decrease across an iron spin-transition at 573 K, while such reduction is ~30–40% smaller than at room temperature, suggesting their Λ are less-affected across the spin-transition under deep-mantle's high temperatures. The temperature dependences of low-spin Λ_{Fp25} and Λ_{Fp75} ($T^{-0.39}$ and $T^{-0.23}$, respectively) are weaker than the conventional $T^{-0.5}$ for high-spin state. If made of Fe-rich oxides (e.g., Fp75), ULVZs should have an ultralow thermal conductivity (~ 3.4 W m^{-1} K^{-1}). Such strong thermal insulation enhances local temperature, vitalizing regional mantle dynamics and thermochemical evolution, and growth of thermal plumes. The significant Λ discontinuity across CMB would induce heterogeneous amplitude and pattern of CMB heat-flux, potentially impacting geodynamo and geomagnetic stability.

Seismological studies have identified several heterogeneous structures in the Earth's deep interior, presumably associated with chemical and/or thermal anomalies. These include two continental-scale large low shear-wave velocity provinces (LLSVPs) beneath the Pacific and Africa, and numerous small, typically ~20–50 km thin and a few hundreds of km long patches of ultralow velocity zones (ULVZs) above the core-mantle boundary (CMB), e.g., Refs. 1–4 and references therein. While these enigmatic structures are expected to be closely linked to the thermochemical evolution of our planet, their detailed nature, origin, and evolution remain poorly understood. The ULVZs are of particular interest for their role in the flow of material and energy at the CMB. Compared to the ambient mantle, they feature much lower seismic compressional (V_p) and shear (V_s) velocities up to ~20 and ~50%, respectively, and a higher density up to ~20%[1–4]. Moreover, recent seismic and geodynamic studies suggested that ULVZs may not be restricted to regions located within or at the edge of the LLSVPs; they instead may be globally distributed above the CMB[1,2,4,5], including in high-velocity areas associated with slab subduction[6]. ULVZs are likely to affect regional mineralogy, geochemistry, and dynamics. In particular, because they directly sit on the CMB, they may partly control the local CMB heat flux (Q_{CMB}) and chemical interactions/reactions between the solid rocky mantle and liquid metallic core.

Though the origin of ULVZs remains an open question, mineralogical, seismological, and geodynamical studies mostly favor ULVZs made of partial melts[4,7–9] and/or iron (Fe)-rich minerals, e.g., Fe-rich (Mg,Fe)O (magnesiowüstite)[10,11], Fe-rich post-perovskite (pPv)[12], and/or

[1]Institute of Earth Sciences, Academia Sinica, Nankang, Taipei, Taiwan. [2]Department of Geosciences, National Taiwan University, Taipei, Taiwan. [3]Department of Earth and Environmental Sciences, Michigan State University, East Lansing, MI, USA. [4]Department of Earth, Environmental, and Planetary Sciences, Northwestern University, Evanston, IL, USA. [5]Bayerisches Geoinstitut, University of Bayreuth, Bayreuth, Germany. ✉e-mail: wphsieh@earth.sinica.edu.tw

pyrite-structured FeO_2H_x[13]. The disordered atomic arrangements in the partial melts and/or the enrichment of relatively heavy Fe atoms in the candidate materials considerably reduce their seismic velocity and increase their density relative to typical mantle lithologies. Furthermore, because the amplitude of velocity reduction and density increase vary from one ULVZ to another[2,4], the exact composition of ULVZs may also be variable, composed of one of the individual candidates or a mixture of them.

Thermal conductivity of deep Earth materials crucially determines the heat flow and temperature profile in the regions where they are present, particularly at the CMB, where heat is extracted from the core predominantly by conduction. Precise determination of the thermal conductivity of ULVZ materials (Λ_{ULVZ}) at CMB's high pressure-temperature (P-T) conditions offers fundamental insights and constraints on the local Q_{CMB}. The Λ_{ULVZ} may further influence spatio-temporal variations in the thermal state at the lowermost mantle, impacting the thermochemical structure and dynamics at both sides of the CMB. However, due to the challenges and limitations of previous experimental and computational methods, very few data for the Λ_{ULVZ} at deep mantle's high P-T conditions are available. Prior measurements on the thermal conductivity of $(Mg_{1-x},Fe_x)O$, $\Lambda_{(Mg,Fe)O}$, largely focused on $x \le 0.2$, representing average mantle. Available data for Fe-rich (Mg,Fe)O, a candidate ULVZ material, with $x \ge 0.5$ (Fe-enrichment potentially found in ULVZs) are rare, e.g., Refs. 14–16 and references therein. Moreover, the previous measurements were either fixed at 300 K up to ~120 GPa[14], or limited to relatively low P-T conditions, e.g., ~1000 K and 23 GPa[15]. Thermal conductivity of Fe-rich (Mg,Fe)O at higher P-T conditions of the deep mantle remains largely unknown. Such deficiency could lead to unreliable modelling of $\Lambda_{(Mg,Fe)O}$ to the lowermost mantle conditions with potentially large uncertainty. In addition, it has been well documented that a pressure-induced spin transition of iron occurs in (Mg,Fe)O at ~40–80 GPa, depending on the FeO content and temperature condition, e.g., Refs. 17–19. Through the spin transition, several physical properties, in particular, density, elastic constants, and thermal conductivity, can be altered[14,17–20], which could in turn affect the deep-mantle dynamics, thermochemical state, and seismic features[19–21]. However, the effects of spin state on the high P-T thermal conductivity of Fe-rich (Mg,Fe)O and on its temperature dependence have never been investigated.

Here, we experimentally demonstrate that the thermal conductivity of polycrystalline $(Mg_{0.75},Fe_{0.25})O$, Λ_{Fp25}, and Fe-rich $(Mg_{0.25},Fe_{0.75})O$, Λ_{Fp75}, at an elevated temperature of 573 K both decrease across the spin transition. The temperature dependences of Λ_{Fp25} and Λ_{Fp75} in low-spin state are both weaker (less sensitive to temperature change) than in high-spin state, indicating the impacts of spin state on the $\Lambda_{(Mg,Fe)O}$ at mantle-relevant conditions. Our data modelling shows that if they are made of Fe-rich oxides, e.g., Fp75, ULVZs should have an ultralow thermal conductivity. Such a feature would not only promote the accumulation of heat and the formation of mantle plumes, but also enhance the dynamics and thermochemical instability at both sides of the CMB. The spatiotemporal evolution of the globally distributed, thermally-insulating ULVZ patches would then alter the local CMB topography and heat flux, potentially influencing the strength and polarity of the geomagnetic field over the Earth's history.

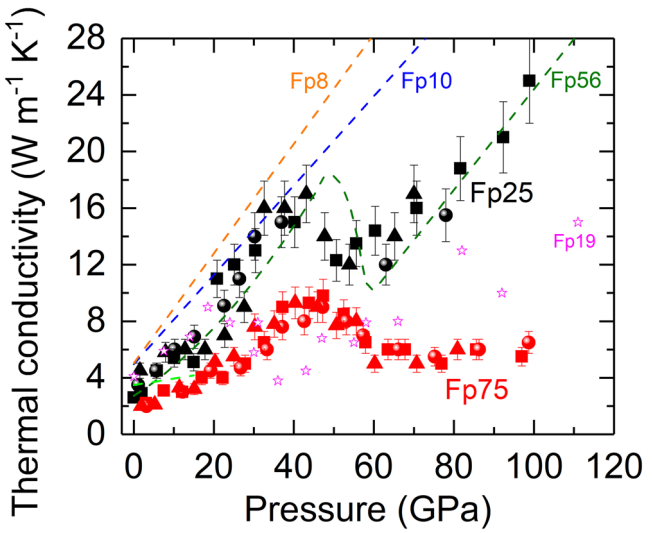

Fig. 1 | Pressure dependence of Λ_{Fp25} and Λ_{Fp75} for polycrystalline oxides at room temperature. Though Λ_{Fp25} (black symbols) and Λ_{Fp75} (red symbols) both initially increase with compression, they present different pressure evolution. Presumably due to the spin transition of iron, the Λ_{Fp25} decreases by ~30% at P ~ 43–54 GPa, while the Λ_{Fp75} decreases by a larger extent of ~45% at higher pressures of P > ~ 53 GPa. In the low-spin state, the Λ_{Fp75} has a much smaller pressure slope than the Λ_{Fp25}. Each symbol shape represents individual measurement run. The vertical bar at each datum point indicates the data uncertainty of ~10–15%. Literature results for single-crystalline Fp8 (orange dashed curve)[14], Fp10 (blue dashed curve)[14], and Fp56 (green dashed curve)[14], as well as sintered polycrystalline Fp20 (bright green dashed line from ambient to 15 GPa)[15] and Fp19 (magenta open stars)[25] are plotted for comparison.

Results and discussion

Thermal conductivity of Fp25 and Fp75 at high pressure and room temperature

We used ultrafast time-domain thermoreflectance (TDTR) coupled with diamond-anvil cells (DACs) to precisely measure Λ_{Fp25} and Λ_{Fp75} to ~100 GPa at room temperature. TDTR has been widely employed to measure the thermal conductivity of various materials with high precision at various high P-T conditions (Refs. 14,22–24 and Methods). The unit-cell volume and spin state of Fp75 have also been complementarily characterized by synchrotron X-ray diffraction (Supplementary Note S1). As shown in Fig. 1, Λ_{Fp25} (black symbols) starts from ~2.6 W m^{-1} K^{-1} at ambient conditions and increases with pressure until 43.1 GPa, after which it decreases by ~30% at ~54 GPa, presumably due to the pressure-induced spin transition of iron[19]. Upon further compression, the low-spin Λ_{Fp25} resumes increasing with higher pressure, reaching ~25 W m^{-1} K^{-1} at 99 GPa.

In contrast, Λ_{Fp75} (red symbols) is systematically lower than Λ_{Fp25}, presumably resulting from the higher FeO content and $Fe^{3+}/\sum Fe$ (see Methods), which induce stronger phonon-impurity and phonon-defect scatterings, respectively, with larger resistance to heat transport. At ambient conditions, Λ_{Fp75} is ~1.9 W m^{-1} K^{-1}, ~27% lower than Λ_{Fp25}. Under compression, Λ_{Fp75} increases much less with increasing pressure than Λ_{Fp25}, and reaches a much lower peak value of ~8.5 ± 1 W m^{-1} K^{-1} at P ~ 40–53 GPa. Afterwards, the Λ_{Fp75} decreases by a larger extent (~45%) and then remains approximately constant, showing a "sluggish" variation at a higher-pressure range than Fp25 through the spin transition. Finally, the low-spin Λ_{Fp75} only increases to ~6.5 W m^{-1} K^{-1} at 99 GPa, ~4-fold lower than Λ_{Fp25} at similar pressures.

We note that several factors could affect the Λ_{Fp}, including FeO content and ferric iron ratio ($Fe^{3+}/\sum Fe$) (representing impurity and defect in the crystal), and grain size. The Fp8, Fp10, and Fp56 samples in Ref. 14 are single crystals with minor amounts of ferric iron, while the Fp25 and Fp75 samples in the present study are polycrystalline powders with ~6 and ~12% ferric iron, respectively (see Methods). At ambient conditions, the Λ_{Fp56} is expected to be lower than Λ_{Fp25}, e.g., Ref. 25. However, our data (Fig. 1) show that the present Λ_{Fp25} seems to be comparable to the literature Λ_{Fp56} up to ~100 GPa, but with slightly lower onset pressure for the Λ reduction across the spin transition. Compared to the literature Fp56 sample, the lower FeO content yet with ~6% ferric iron in the present Fp25 sample may have counterbalanced the opposite effects between FeO content (the fewer FeO, the smaller thermal resistance due to less impurity scattering) and ferric

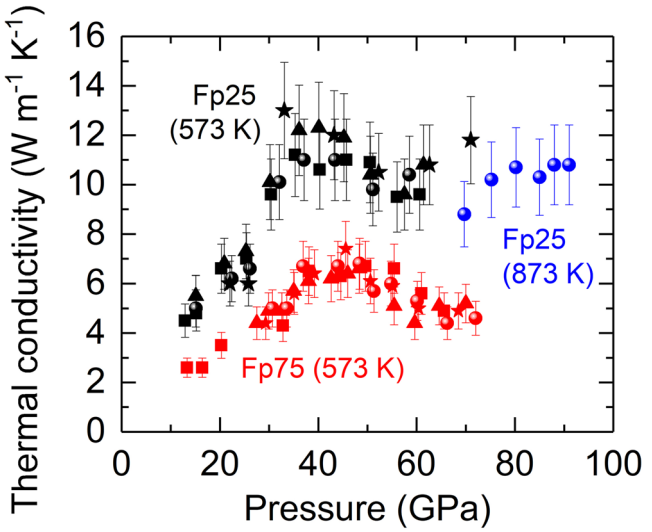

Fig. 2 | Pressure dependence of the Λ_{Fp25} and Λ_{Fp75} at elevated temperatures. Compared to the pressure evolution at room temperature, the Λ_{Fp25} (black symbols) and Λ_{Fp75} (red symbols) at 573 K both soften in a more sluggish and gentle manner across the spin transition, where the pressure interval shifts to slightly higher pressures. The low-spin Λ_{Fp25} at 873 K (blue symbols) has a weaker pressure slope than at room temperature. Each symbol shape represents individual experimental run. The vertical bar at each datum point shows its uncertainty of ~10–15%.

iron (the more ferric iron, the larger thermal resistance due to more defects), leading to comparable thermal conductivity. The much lower Λ_{Fp75} along with a weaker pressure dependence in high-spin state (its low-spin state even plateaus) is therefore presumably due to the large amounts of FeO and ferric iron. In addition, using electron backscattered diffraction we found that the typical grain size of present polycrystalline Fp25 and Fp75 samples before and after high-pressure measurements were both ~15–40 μm, comparable or larger than our laser spot size in TDTR thermal conductivity measurements. We thus expect that the grain boundary plays minor roles here in affecting their thermal conductivity. Understanding the detailed, fundamental mechanisms for thermal transport in these samples in high- and low-spin states requires further advanced theoretical and computational studies.

Λ_{Fp25} and Λ_{Fp75} across the spin transition at elevated temperatures

To assess how elevated temperature influences Λ_{Fp25} and Λ_{Fp75} across the spin transition, we first compressed the sample to ~10 GPa and heated it up to 573 K (300 °C) using an externally-heated DAC (EHDAC). We then measured Λ at 573 K from ~12 to 72 GPa across the spin transition. As shown in Fig. 2, Λ_{Fp25} at 573 K (black symbols) initially increases with pressure from 12.9 to ~35 GPa and, given the data uncertainty of ~10–15%, remains at ~11.5 ± 1 W m^{-1} K^{-1} between 35 and 46 GPa. We then observed a slight decrease (~17%) until ~56 GPa, after which the Λ_{Fp25} re-increases with pressure to ~11.8 W m^{-1} K^{-1} at 71 GPa. Overall, in contrast to the behavior at room temperature through the spin transition (Fig. 1), the Λ_{Fp25} at 573 K is systematically lower, with a plateau and fairly gentle decrease over a wider pressure range (~35–56 GPa). In addition, to explore its pressure dependence in the low-spin state, we have further measured the Λ_{Fp25} at 873 K (blue symbols) in a separate experimental run, which shows a smaller pressure slope than at room temperature. Finally, Λ_{Fp75} (red symbols) at 573 K is, again, systematically lower than the Λ_{Fp25}, with a plateau at ~6.5 ± 0.5 W m^{-1} K^{-1} at higher pressures of ~38–50 GPa. We also observed a sluggish decrease (~30%) to ~4.6 W m^{-1} K^{-1} until ~66 GPa. Though our measurement pressure was only extended to 72 GPa, the low-spin Λ_{Fp75} seems to have a weak pressure dependence as that at room temperature.

Since the Λ of a material scales with the square of its sound velocity[14,26] (proportional to elastic constants), the pressure evolution of Λ_{Fp25} and Λ_{Fp75} in Figs. 1 and 2 can be primarily accounted for by the softening of elastic constants across the spin transition[14,18]. Moreover, compared to room temperature, the extent of decrease in Λ through the spin transition at 573 K is more sluggish, and the transition extends to higher pressures. These observations are in good agreement with the qualitative evolution of elastic constants across the spin transition at elevated temperatures as predicted by ab initio calculations[18,19].

Temperature dependence of the low-spin Λ_{Fp25} and Λ_{Fp75}

Understanding the temperature dependence of Λ_{Fp25} and Λ_{Fp75} in the low-spin state is critical to better constrain the deep-mantle thermal state. To this end, we explored how the low-spin Λ_{Fp25} and Λ_{Fp75} change with temperature to ~973 K (Fig. 3). To quantify their temperature dependence, for simplicity, we assumed that the transition to the low-spin state is complete above ~62–64 GPa and that low-spin Λ_{Fp25} and Λ_{Fp75} can be modelled as $\Lambda(T) = \Lambda_{LS} T^{n}$, where Λ_{LS} is a normalization constant. Such a power law dependence for Λ(T) is based on fundamental heat transport theory under Debye approximation and on an assumption that the three phonon umklapp scattering between acoustic phonons is the predominant mechanism for heat transport[27–30]. Since phonon relaxation time can be approximated to be inversely proportional to T, heat transport theory predicts that for a pure crystal, Λ(T) would scale with T^{-1}, while for an impurity-bearing crystal, Λ(T) would scale with $T^{-0.5}$, see Refs. 27–30 for detailed derivations of the theory for thermal conductivity at high temperatures. We determined the temperature exponent n by linearly fitting a regression line in the lnΛ-lnT plot. For low-spin Λ_{Fp25}, we found n = −0.36(± 0.07) at P = 62–68 GPa and n = −0.41(± 0.06) at P = 72–78 GPa (Fig. 3a), slightly weaker (less sensitive to temperature change) than the typical $T^{-0.5}$ dependence for several Fe-bearing mantle minerals[14,15,31–34]. Note that despite the spin state, $\Lambda_{(Mg,Fe)O}(T)$ has been conventionally approximated to $T^{-0.5}$ throughout the whole mantle[14,15,31,33], although a $T^{-0.24}$ dependence for high-spin Fp5 and Fp20 only up to 14 GPa and ~1150 K had once been reported[30]. Furthermore, the Λ_{Fp75} has a much weaker temperature dependence with n ranging from −0.15(± 0.04) to −0.3(± 0.07), see Fig. 3b. We emphasize that our findings represent critical experimental results indicating a weaker temperature dependence for the low-spin Λ_{Fp25} and Λ_{Fp75} than conventionally thought. We use this result to update modelled values for the deep-mantle conditions (see discussion below).

Modelling the thermal conductivity of lower mantle minerals along a mantle geotherm

Our results for Λ_{Fp25} and Λ_{Fp75} with different P, T, and FeO content provide better constraints on the thermal conductivity profiles of (Mg,Fe)O and pyrolitic mantle, which in turn play a key role in the thermochemical evolution and dynamics in the deep mantle, including the impacts on LLSVPs and ULVZs. Here we first modelled Λ_{Fp25} and Λ_{Fp75} along a representative mantle geotherm[35], to which we added a steep temperature rise from 2587 K at 2800 km depth (~130 GPa)[35] to 4000 K at the CMB (~136 GPa). Furthermore, we assumed that the Λ(T) of high-spin Λ_{Fp25} and Λ_{Fp75} follow the typical $T^{-0.5}$, while in the low-spin state they follow the trend we found in Fig. 3—i.e., Λ_{Fp25} scales with $T^{-0.39}$ and Λ_{Fp75} scales with $T^{-0.23}$. In the mixed-spin state, Λ(T) is approximated as the average of the high- and low-spin states. We find that Λ_{Fp25} (black solid line in Fig. 4a) starts from ~4 W m^{-1} K^{-1} at 660 km and increases with depth, followed by a slight decrease across the spin transition at ~1000–1400 km depth. The low-spin Λ_{Fp25} then reaches ~11.5 W m^{-1} K^{-1} at 2800 km depth, and slightly reduces to 10 W m^{-1} K^{-1} at the CMB due to the steep temperature rise. Compared to the

https://doi.org/10.1038/s41467-025-65430-7

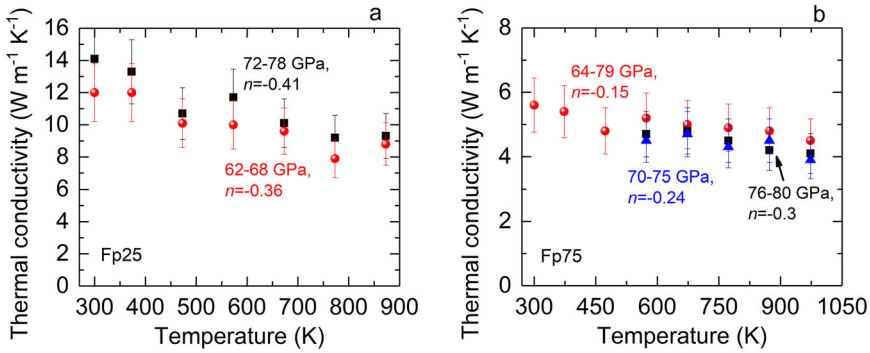

Fig. 3 | Temperature dependence of Λ_{Fp25} and Λ_{Fp75} in the low-spin state. a Λ_{Fp25} has a temperature dependence T^{n} with n = −0.36 to −0.41, which is slightly weaker than the typical $T^{-0.5}$ for Fe-bearing mantle minerals[14,15,31–34]. **b** Λ_{Fp75} shows an even smaller temperature exponent of −0.15 to −0.3 at deep-mantle pressures. The vertical bar at each datum point represents its uncertainty of ~15%. The thermal pressure has minor effects on the temperature dependence, see Supplementary Note S2 for details.

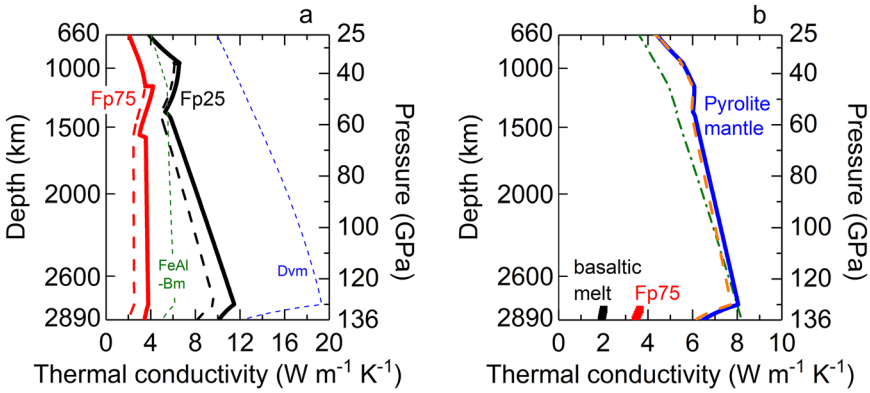

Fig. 4 | Modelled thermal conductivity profiles of lower mantle minerals along a representative mantle geotherm. a The red solid line represents the Λ_{Fp75} with a conventional $T^{-0.5}$ dependence for high-spin state and a weaker $T^{-0.23}$ dependence as we experimentally found for low-spin state, while, for comparison, the red dashed line indicates the Λ_{Fp75} with the conventional $T^{-0.5}$ dependence for both high- and low-spin states. The black solid line shows the Λ_{Fp25} with the conventional $T^{-0.5}$ dependence for high-spin state and a weaker $T^{-0.39}$ dependence for low-spin state; the black dashed line is the Λ_{Fp25} with the conventional $T^{-0.5}$ dependence for both high- and low-spin states. Overall, both Λ_{Fp25} and Λ_{Fp75} increase with depth, except for the range where the spin transition occurs. The low-spin Λ_{Fp75} remains nearly a constant of ~3.6–3.8 W m^{-1} K^{-1} due to its weak temperature dependence. The small artifact discontinuities at the start and end of the spin transition result from the assumed temperature dependence in the mixed-spin state. Profiles of $\Lambda_{FeAl\text{-}Bm}$ (FeAl-Bm, green dashed line) and $\Lambda_{davemaoite}$ (Dvm, blue dashed line) are plotted for comparison. **b** From the top to the bottom of the lower mantle, the Λ_{LM} (blue solid line) increases two fold and converges to the previously modelled one (green dash-dotted line)[14] at 8 W m^{-1} K^{-1} at the lowermost mantle. The sudden decrease in Λ profile above the CMB is due to the steep temperature rise.

conventionally assumed $T^{-0.5}$ for both high- and low-spin states (black dashed line), the weaker temperature-dependence in the low-spin state ($T^{-0.39}$) we found yields an ~20% higher Λ_{Fp25} at the lowermost mantle. Moreover, we highlight that the Λ_{Fp75} (red solid line) remains as low as ~3.6–3.8 W m^{-1} K^{-1} from ~1600–2800 km depth (~ 50% higher than that with the conventional $T^{-0.5}$ dependence, red dashed line). The CMB's high temperature further decreases the Λ_{Fp75} to an exceptionally low value of ~3.4 W m^{-1} K^{-1}.

Figure 4a also shows our modelled Λ profile of (Fe,Al)-bearing bridgmanite (FeAl-Bm) with an assumed $T^{-0.5}$ dependence[33] (FeAl-Bm, green dashed line) and $CaSiO_3$ davemaoite with a $T^{-1.1}$ dependence[36] (Dvm, blue dashed line). Combining these two profiles with our Λ_{Fp25} and using a Voigt-Reuss-Hill (VRH) volumetric average scheme then provide an estimate of the thermal conductivity of pyrolitic lower-mantle aggregate, Λ_{LM}. Based on the pyrolite model, the lower mantle is composed of FeAl-Bm (~ 75 vol%), (Mg,Fe)O (~ 18 vol%), and $CaSiO_3$ davemaoite (~ 7 vol%), and for calculations we assume $\Lambda_{LM} = 0.75\Lambda_{FeAl\text{-}Bm} + 0.18\Lambda_{Fp25} + 0.07\Lambda_{davemaoite}$. At ~1000 km depth, our present modelled Λ_{LM} (blue solid line in Fig. 4b) is ~22% higher than the previously modelled profile based on room-temperature data (green dash-dotted line in Fig. 4b with a potential temperature of 2500 K[14]). Nevertheless, these two lines gradually converge in the deep mantle. Our modelled profile reaffirms that with the davemaoite, Λ_{LM} is ~8 W m^{-1} K^{-1}[14] at ~2800 km depth, but decreases to ~6.5 W m^{-1} K^{-1} at the CMB, consistent with previous results, e.g., Refs. 37,38. For comparison, we also modelled a Λ_{LM}, where the Λ_{Fp} instead follows the conventional $T^{-0.5}$, despite its spin state (orange dashed line in Fig. 4b). Because the (Mg,Fe)O only contributes ~18 vol%, the Λ_{LM} with different $\Lambda_{(Mg,Fe)O}(T)$ in the low-spin state only differs by <4% throughout the deep mantle. For similar reasons, the variable FeO content in the (Mg,Fe)O with depth also has a minor effect on the modelled Λ_{LM}[14]. Finally, the Λ_{LM} is insensitive to the average scheme we adopted: when using Hashin–Shtrikman scheme[14], the modelled Λ_{LM} is comparable (< ~10–15% difference) to that using the VRH scheme throughout the lower mantle.

Impacts of thermally-insulating ULVZs on the lower-mantle thermal structure and dynamics and geodynamo evolutions

The anomalously low velocities and higher density of ULVZs relative to ambient mantle imply that they are likely thermochemical heterogeneities[1,2,5], e.g., Fe-rich mantle minerals, partial melts, or subducted slab materials. If made of Fe-rich oxides[10,11], e.g., Fp75, ULVZs would have an exceptionally low thermal conductivity, Λ_{ULVZ}, ~3.4 W m^{-1} K^{-1} (red short stripe above 2890 km depth in Fig. 4b). This

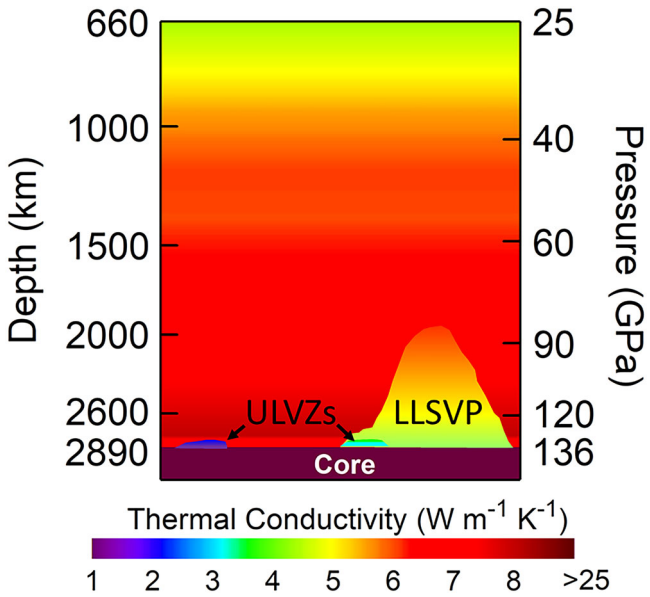

Fig. 5 | Illustration for the modelled thermal conductivity in the lower mantle. The profiles for the pyrolitic lower mantle and representative LLSVP, respectively, are from present study and Ref. 39. A ULVZ made of Fp75 and basaltic melt has an ultralow thermal conductivity of ~3.4 W m^{-1} K^{-1} and ~1.9 W m^{-1} K^{-1}, respectively. A significant thermal conductivity discontinuity across the CMB is present, in particular between the ULVZ and core.

conductivity would further decrease with higher FeO content and thus, ULVZs may locally act as a thermal insulator at the CMB, meaning first that the amount of heat flowing from the core to the mantle may be limited at ULVZs locations, and second that ULVZs may have remained hot compared to their surroundings. Estimating temperature excess within ULVZs requires numerical simulations of mantle dynamics. Such excess potentially reaches several tens to a few hundreds of degrees, as suggested by temperature excess within low conductivity LLSVPs[39]. Such low conductivity is comparable to the previously modelled Fe-rich mantle aggregate[14]. Based on the results of Ref. 40, we further modelled thermal conductivity of basaltic melt at CMB-relevant high P-T conditions to be ~1.9 W m^{-1} K^{-1} (black short stripe above 2890 km depth in Fig. 4b). This value should be considered an upper bound relative to thermal conductivity of Fe-enriched melt[40]. If formed by heavy melt patches originated from the remnants of basal magma ocean[41,42] or subducted slabs[4,7], ULVZs have not only ultralow seismic velocities, but also ultralow thermal conductivity, typically about 3-fold lower than the ambient mantle.

The different thickness and amplitude of velocity and density anomalies among ULVZs observed at different locations[2,4] may imply that they result from distinct formation mechanisms or are composed of different combinations of candidate materials. Recent seismic studies suggest that the internal structure of ULVZs may be complex with chemical heterogeneity and/or multilayer structures[41,43], making it difficult to resolve the spatial changes in the thermal conductivity within individual ULVZ. Nevertheless, since ULVZs are small-sized and share common features of Fe-enrichment and low-velocity, these properties coherently reduce their ability to conduct heat. We thus expect that the ultralow Λ_{ULVZ} we modelled based on that of Fp75 and basaltic melt (Fig. 4b) should be reasonably representative of Λ_{ULVZ}, although, again, different ULVZs may have different origin and nature.

Our findings have important consequences on the evolution of the CMB region. The ultralow Λ_{ULVZ} with strong thermal insulating effect would promote accumulation of heat (and temperature) at their base, thus delaying cooling, which in turn further reduces Λ, as the Λ decreases with higher temperature (Fig. 3). This positive feedback mechanism results in thermal runaway that raises the local temperature, enhancing the buoyancy of ULVZs, their interactions with the surrounding LLSVPs and mantle, as well as the formation of thermal plumes rooted in ULVZs. Meanwhile, the large radial temperature gradient across the thin ULVZ patches caused by the efficient thermal insulation could produce a local, relatively cooler condition above them. Such reduced temperature may facilitate the growth of pPv above the ULVZs, and induce small-scale lateral thermal instability that could alter the regional mantle dynamics. Moreover, the thermal conductivity of the outer core, depending on its composition and investigation methods, has been suggested to a wide range of ~25–250 W m^{-1} K^{-1}, e.g., Refs. 24,44,45 and references therein. Thus, within ULVZs, thermal conductivity on the mantle side of the CMB would be much lower than that on the outermost core side (Fig. 5) by at least one-order-of-magnitude. Combined with a high ULVZ temperature, T_{ULVZ}, this may significantly depress the local Q_{CMB}. Furthermore, if T_{ULVZ} is higher than the CMB temperature, local patches of negative Q_{CMB}, where heat flows from the mantle to the core, may be triggered. Such patches could in turn influence core flow, at least locally. Patches of very low or negative Q_{CMB} would further strongly increase the amplitude of lateral variations in Q_{CMB}, increasing the Q^* parameter[33] (defined as the ratio between the amplitude in Q_{CMB} lateral variations and twice the difference between the horizontally average Q_{CMB} and the core adiabatic heat flux). These effects would then impact the spatial and temporal evolution of the geodynamo, including the timing between polarity reversals of geomagnetic field[46]. Future direct experimental measurements on the thermal conductivity of (Mg,Fe)O and other candidate ULVZ materials under deep-mantle's high P-T conditions will enable assessment of the validity of our modelled conductivity profiles and offer crucial insights to the heat transport at the lowermost mantle. Coupled with advanced numerical modelling that considers the effects of deep-mantle heterogeneities (e.g., LLSVPs, ULVZs, and slabs), these studies should bring better constraints on the complex evolution of lower-mantle thermochemical structures, the formation and growth of plumes, changes in the CMB heat flux pattern, and the stability of geodynamo.

Methods

Sample synthesis and characterization

Polycrystalline powder samples of $(Mg_{0.75},Fe_{0.25})O$—Fp25 and $(Mg_{0.25},Fe_{0.75})O$—Fp75 were synthesized by reacting fine MgO (99.95%, -325 Mesh from Alfa Aesar) and Fe_2O_3 (99.9% from Alfa Aesar) powders inside a vertical tube furnace at 1300 °C and an oxygen fugacity of approximately 10^{-10} atm, roughly following the methods in Ref. 47. Powders reacted inside the furnace for two 24 h rounds, re-mixing the powder in between each round to promote sample homogeneity. Powder X-ray diffraction confirmed the formation of (Mg,Fe)O and the absence of any magnesioferrite peaks.

We determined the exact chemical composition of the Fp25 and Fp75 samples to be $(Mg_{0.75}Fe_{0.25})O$ and $(Mg_{0.25}Fe_{0.75})O$, respectively, using an electron probe microanalyzer in Academia Sinica. We further characterized their relative ferric iron content ($Fe^{3+}/\sum Fe$) by in-house Mössbauer spectroscopy in Bayerisches Geoinstitut. Mössbauer spectra were obtained at room temperature in transmission mode using a constant acceleration Mössbauer spectrometer, with a nominal 370 MBq ^{57}Co point source in a 12 μm Rhodium matrix. The velocity scale was calibrated using a 25 μm thick α-Fe foil. Samples were loaded into 1 mm diameter sample holders. The spectra were collected for 3–5 days, then folded and fitted using the program MossA[48] with multiple pseudo-Voigt line shapes and linear baseline correction. The $Fe^{3+}/\sum Fe$ is ~6% in Fp25 and ~12% in Fp75, respectively, see Supplementary Note S4 for more details.

Sample preparation for high pressure experiments

To perform high-pressure thermal conductivity measurements, we first manually polished the (Mg,Fe)O samples to ~15 μm thick, and thermally evaporated an aluminum (Al) film (~ 90 nm thick) on the samples. We then loaded the sample of interest, together with a ruby sphere, into a symmetric piston-cylinder diamond anvil cell (DAC) with a pair of 200 μm culets and a rhenium gasket. For room temperature experiments, we used silicone oil (CAS No. 63148-62-9 from ACROS ORGANICS) as the pressure medium. We calibrated the pressure within the sample chamber by measuring the ruby's R_1 fluorescence peak as a function of pressure[49] (uncertainty of ~0.1–0.2 GPa). The sample geometry within the DAC and experimental set-up are essentially the same as in our recent studies, see, e.g., Refs. 34,50.

For simultaneous high P-T thermal conductivity measurements, we switched to externally-heated DAC (EHDAC), which is composed of a BX-90 diamond cell coupled with a home-made resistive heater placed next to the sample chamber. Such setup offers a homogeneous high temperature environment over the sample chamber. Here we used MgO nanopowder (CAS No. 1309-48-4 from Merck with a typical grain size ≤50 nm) as the pressure medium, with advantages of (1) a thermal conductivity of ~3–4 $W\,m^{-1}\,K^{-1}$ from ambient to ~100 GPa, much lower than other typical solid pressure media, due to its very small grain size, and (2) easy access when loading (compared to high-pressure gas loading). Moreover, we added a gas membrane in the EHDAC to in situ manipulate the experimental pressure during our high P-T measurements. The heating-induced broadening of ruby's R1 peak leads to a pressure uncertainty of ~0.1–0.5 GPa. The assemblage of our EHDAC and pressure uncertainty were detailed in Refs. 51,52. Finally, we note that after the high P-T measurements we checked the composition of recovered samples (Fp25 and Fp75) by energy-dispersive X-ray spectroscopy and confirmed that the FeO content in each sample remains essentially the same with a slight variation of <1–2 at. %.

Thermal conductivity measurements

We employed time-domain thermoreflectance (TDTR), a well-developed ultrafast optical pump-probe technique[22,53], to precisely measure the thermal conductivity of Fp25 and Fp75 at high pressure and a wide range of temperature conditions. Details of the TDTR setup and operation principles were described in, for example, Refs. 23,53. We have applied the same experimental method to study the thermal conductivity of numerous geomaterials in the Earth and planetary interiors[14,24,33,34,50,54,55]. In brief, we split the output of an ultrafast Ti:sapphire oscillator laser into pump and probe beams. The pump beam heated the Al film evaporated on the (Mg,Fe)O sample, creating variations in temperature and optical reflectivity on the Al's surface, which were then probed by the probe beam at a series of delayed time. The temporal changes in the reflected probe beam intensity were recorded by a fast silicon photodiode along with a lock-in amplifier.

To determine the thermal conductivity of the (Mg,Fe)O sample at variable P-T conditions, we fit the TDTR data—ratio of the in-phase signal V_{in} to out-of-phase V_{out} ($-V_{in}/V_{out}$) with thermal model calculations that simulate the dynamics of bi-directional heat flow from the Al film to the sample and pressure medium[23,56]. Supplementary Fig. S3 shows a representative TDTR spectrum for Fp75 at 97 GPa and room temperature along with the fitting by the bi-directional thermal model calculations. Note that in our data analysis, the thickness of Al film and volumetric heat capacity of (Mg,Fe)O are two important parameters that would influence the derived thermal conductivity of (Mg,Fe)O. We adopted a recently developed method from Ref. 40 to estimate the thickness of Al at high P-T conditions. As for the heat capacity of Fp25 and Fp75, since they are not well-known, we assumed they are similar to the Fp18.75 (Ref. 17) and Fp56 (Ref. 14), respectively, given the similar FeO contents. We emphasize that the uncertainty in thermal conductivity we report for (Mg,Fe)O is dominated by analysis uncertainty, rather than measurement uncertainty. Following the approaches described in Refs. 57,58, we further estimated the data uncertainty by evaluating the total uncertainties translated from all the input parameters in the thermal model calculations, see Supplementary Figs. S3 and S4. The error is ~10% at P < 50 GPa and ~10–15% at P = 50–100 GPa.

Data availability

The main data generated in this study are available in https://zenodo.org/records/17284226.

References

1. McNamara, A. K. A review of large low shear velocity provinces and ultra low velocity zones. *Tectonophysics* **760**, 199–220 (2019).
2. Yu, S. & Garnero, E. J. Ultralow velocity zone locations: a global assessment. *Geochem. Geophys. Geosyst.* **19**, 396–414 (2018).
3. Garnero, E. J., Revenaugh, J., Williams, Q., Lay, T. & Kellogg, L. H. Ultralow velocity zone at the core-mantle boundary. *Geodynamics* **28**, 319 (1998).
4. Hansen, S. E., Garnero, E. J., Li, M., Shim, S. H. & Rost, S. Globally distributed subducted materials along the Earth's core-mantle boundary: implications for ultralow velocity zones. *Sci. Adv.* **9**, eadd4838 (2023).
5. Li, M., McNamara, A. K., Garnero, E. J. & Yu, S. Compositionally-distinct ultra-low velocity zones on Earth's core-mantle boundary. *Nat. Commun.* **8**, 177 (2017).
6. Su, Y. et al. Detections of ultralow velocity zones in high-velocity lowermost mantle linked to subducted slabs. *Nat. Geosci.* **17**, 332–339 (2024).
7. Wolf, J., Long, M. D. & Frost, D. A. Ultralow velocity zone and deep mantle flow beneath the Himalayas linked to subducted slab. *Nat. Geosci.* **17**, 302–308 (2024).
8. Andrault, D. et al. Melting of subducted basalt at the core-mantle boundary. *Science* **344**, 892 (2014).
9. Pradhan, G. K. et al. Melting of MORB at core-mantle boundary. *Earth Planet Sci. Lett.* **431**, 247–255 (2015).
10. Wicks, J. K., Jackson, J. M. & Sturhahn, W. Very low sound velocities in iron - rich (Mg, Fe) O: implications for the core - mantle boundary region. *Geophys. Res. Lett.* **37**, L15304 (2010).
11. Wicks, J. K., Jackson, J. M., Sturhahn, W. & Zhang, D. Sound velocity and density of magnesiowüstites: implications for ultralow-velocity zone topography. *Geophys. Res. Lett.* **44**, 2148 (2017).
12. Mao, W. L. et al. Iron-rich post-perovskite and the origin of ultralow-velocity zones. *Science* **312**, 564–566 (2006).
13. Liu, J. et al. Hydrogen-bearing iron peroxide and the origin of ultralow-velocity zones. *Nature* **551**, 494–497 (2017).
14. Hsieh, W. P., Deschamps, F., Okuchi, T. & Lin, J. F. Effects of iron on the lattice thermal conductivity of Earth's deep mantle and implications for mantle dynamics. *Proc. Natl. Acad. Sci. USA* **115**, 4099–4104 (2018).
15. Zhang, Y., Yoshino, T. & Osako, M. Effect of iron content on thermal conductivity of ferropericlase: implications for planetary mantle dynamics. *Geophys Res Lett.* **50**, e2022GL101769 (2023).
16. Hasegawa, A. et al. Composition and pressure dependence of lattice thermal conductivity of (Mg,Fe)O solid solutions. *Comptes Rendus - Geosci.* **351**, 229–235 (2019).
17. Wu, Z., Justo, J. F., Da Silva, C. R. S., De Gironcoli, S. & Wentzcovitch, R. M. Anomalous thermodynamic properties in ferropericlase throughout its spin crossover transition. *Phys. Rev. B* **80**, 014409 (2009).
18. Wentzcovitch, R. M. et al. Anomalous compressibility of ferropericlase throughout the iron spin cross-over. *Proc. Natl. Acad. Sci. USA* **106**, 8447–8452 (2009).
19. Lin, J.-F., Speziale, S., Mao, Z. & Marquardt, H. Effects of the electronic spin transitions of iron in lower mantle minerals: implications

for deep mantle geophysics and geochemistry. *Rev. Geophys.* **51**, 244–275 (2013).
20. Badro, J. Spin transitions in mantle minerals. *Annu Rev. Earth Planet Sci.* **42**, 231–248 (2014).
21. Cobden, L. et al. Full-waveform tomography reveals iron spin crossover in Earth's lower mantle. *Nat. Commun.* **15**, 1961 (2024).
22. Zhou, Y., Dong, Z. Y., Hsieh, W. P., Goncharov, A. F. & Chen, X. J. Thermal conductivity of materials under pressure. *Nat. Rev. Phys.* **4**, 319–335 (2022).
23. Hsieh, W. P., Chen, B., Li, J., Keblinski, P. & Cahill, D. G. Pressure tuning of the thermal conductivity of the layered muscovite crystal. *Phys. Rev. B* **80**, 180302 (2009).
24. Hsieh, W. P. et al. Low thermal conductivity of iron-silicon alloys at Earth's core conditions with implications for the geodynamo. *Nat. Commun.* **11**, 3332 (2020).
25. Ohta, K., Yagi, T., Hirose, K. & Ohishi, Y. Thermal conductivity of ferropericlase in the Earth's lower mantle. *Earth Planet Sci. Lett.* **465**, 29–37 (2017).
26. Ashcroft, N. W. & Mermin, N. D. *Solid State Physics*. (Wiley, 1996).
27. Roufosse, M. & Klemens, P. G. Thermal conductivity of complex dielectric crystals. *Phys. Rev. B* **7**, 5379–5386 (1973).
28. Klemens, P. G. Thermal resistance due to point defects at high temperatures. *Phys. Rev.* **119**, 507–509 (1960).
29. de Koker, N. Thermal conductivity of MgO periclase at high pressure: implications for the D" region. *Earth Planet Sci. Lett.* **292**, 392–398 (2010).
30. Manthilake, G. M., de Koker, N., Frost, D. J. & McCammon, C. A. Lattice thermal conductivity of lower mantle minerals and heat flux from Earth's core. *Proc. Natl. Acad. Sci. USA* **108**, 17901–17904 (2011).
31. Deschamps, F. & Hsieh, W. P. Lowermost mantle thermal conductivity constrained from experimental data and tomographic models. *Geophys. J. Int* **219**, S115–S136 (2019).
32. Dalton, D. A., Hsieh, W. P., Hohensee, G. T., Cahill, D. G. & Goncharov, A. F. Effect of mass disorder on the lattice thermal conductivity of MgO periclase under pressure. *Sci. Rep.* **3**, 2400 (2013).
33. Hsieh, W. P., Deschamps, F., Okuchi, T. & Lin, J. F. Reduced lattice thermal conductivity of Fe-bearing bridgmanite in Earth's deep mantle. *J. Geophys Res Solid Earth* **122**, 4900–4917 (2017).
34. Chien, Y. H., Marzotto, E., Tsao, Y. C. & Hsieh, W. P. Anisotropic thermal conductivity of antigorite along slab subduction impacts seismicity of intermediate-depth earthquakes. *Nat. Commun.* **15**, 5198 (2024).
35. Katsura, T. A revised adiabatic temperature profile for the mantle. *J. Geophys Res* **127**, e2021JB023562 (2022).
36. Zhang, Z. et al. Thermal conductivity of CaSiO3 perovskite at lower mantle conditions. *Phys. Rev. B* **104**, 184101 (2021).
37. Stackhouse, S., Stixrude, L. & Karki, B. B. First-principles calculations of the lattice thermal conductivity of the lower mantle. *Earth Planet Sci. Lett.* **427**, 11–17 (2015).
38. Geballe, Z. M., Sime, N., Badro, J., van Keken, P. E. & Goncharov, A. F. Thermal conductivity near the bottom of the Earth's lower mantle: Measurements of pyrolite up to 120 GPa and 2500 K. *Earth Planet Sci. Lett.* **536**, 116161 (2020).
39. Guerrero, J. M., Deschamps, F., Hsieh, W. P. & Tackley, P. J. The combined effect of heterogeneous thermal conductivity, chemical density contrast, and heat-producing element enrichment on the stability of primordial reservoirs above the core-mantle boundary. *Earth Planet Sci. Lett.* **637**, 118699 (2024).
40. Hsieh, W. P., Chang, Y. Y., Tsao, Y. C., Lin, C. H. & Vilella, K. Exceptionally low thermal conduction of basaltic glasses and implications for the thermo-chemical evolution of the Earth's primitive magma ocean. *J. Geophys Res Solid Earth* **129**, e2023JB027722 (2024).
41. Pachhai, S., Li, M., Thorne, M. S., Dettmer, J. & Tkalčić, H. Internal structure of ultralow-velocity zones consistent with origin from a basal magma ocean. *Nat. Geosci.* **15**, 79–84 (2022).
42. Labrosse, S., Hernlund, J. W. & Coltice, N. A crystallizing dense magma ocean at the base of the Earth's mantle. *Nature* **450**, 866–869 (2007).
43. Li, Z., Leng, K., Jenkins, J. & Cottaar, S. Kilometer-scale structure on the core–mantle boundary near Hawaii. *Nat. Commun.* **13**, 2787 (2022).
44. Pozzo, M., Davies, C. J. & Alfè, D. Towards reconciling experimental and computational determinations of Earth's core thermal conductivity. *Earth Planet Sci. Lett.* **584**, 117466 (2022).
45. Landeau, M., Fournier, A., Nataf, H. C., Cébron, D. & Schaeffer, N. Sustaining Earth's magnetic dynamo. *Nat. Rev. Earth Environ.* **3**, 255–269 (2022).
46. Terra-Nova, F. & Amit, H. Regionally-triggered geomagnetic reversals. *Sci. Rep.* **14**, 9639 (2024).
47. Bonczar, L. J. & Graham, E. K. The pressure and temperature dependence of the elastic properties of polycrystal magnesiowustite. *J. Geophys. Res.* **87**, 1061–1078 (1982).
48. Prescher, C., McCammon, C. & Dubrovinsky, L. MossA: a program for analyzing energy-domain Mössbauer spectra from conventional and synchrotron sources. *J. Appl Crystallogr* **45**, 329–331 (2012).
49. Dewaele, A., Loubeyre, P. & Mezouar, M. Equations of state of six metals above 94GPa. *Phys. Rev. B* **70**, 094112 (2004).
50. Hsieh, W. P. et al. reduced thermal conductivity of hydrous aluminous silica and calcium ferrite-type phase promote water transportation to earth's deep mantle. *J. Geophys. Res. Solid Earth* **130**, e2024JB030704 (2025).
51. Hsieh, W.-P. High-pressure thermal conductivity and compressional velocity of NaCl in B1 and B2 phase. *Sci. Rep.* **11**, 21321 (2021).
52. Hsieh, W.-P. et al. Low thermal conductivity of hydrous phase D leads to a self-preservation effect within a subducting slab. *J. Geophys Res Solid Earth* **127**, e2022JB024556 (2022).
53. Cahill, D. G. et al. Nanoscale thermal transport. II. 2003-2012. *Appl Phys. Rev.* **1**, 011305 (2014).
54. Chao, K. H. & Hsieh, W. P. Thermal conductivity anomaly in $(Fe_{0.78}Mg_{0.22})CO_3$ siderite across spin transition of iron. *J. Geophys Res Solid Earth* **124**, 1388–1396 (2019).
55. Hsieh, W.-P., Deschamps, F., Tsao, Y.-C., Yoshino, T. & Lin, J.-F. A thermally conductive Martian core and implications for its dynamo cessation. *Sci. Adv.* **10**, eadk1087 (2024).
56. Schmidt, A., Chiesa, M., Chen, X. & Chen, G. An optical pump-probe technique for measuring the thermal conductivity of liquids. *Rev. Sci. Instrum.* **79**, 064902 (2008).
57. Zheng, X., Cahill, D. G., Krasnochtchekov, P., Averback, R. S. & Zhao, J. C. High-throughput thermal conductivity measurements of nickel solid solutions and the applicability of the Wiedemann-Franz law. *Acta Mater.* **55**, 5177–5185 (2007).
58. Cahill, D. G. & Watanabe, F. Thermal conductivity of isotopically pure and Ge-doped Si epitaxial layers from 300 to 550 K. *Phys. Rev. B* **70**, 235322 (2004).

Acknowledgements

This work was partially supported by the Academia Sinica and the National Science and Technology Council (NSTC) of Taiwan, Republic of China, under Contract AS-IA-111-M02 (to W.P.H.), 113-2628-M-001-013- (to W.P.H.), AS-IA-113-M02 (to F.D.), and 113-2116-M-001-021 (to F.D.). S.M.D. acknowledges support from the US National Science Foundation EAR-2310829. A. Pease and H. Bausch were supported by the US Department of Energy, National Nuclear Security Administration, through the Chicago/DOE Alliance Center (DE-NA0003975). We thank Prof. E. Ohtani for fruitful discussions and assistance on the sample

analysis. F.W. is funded by the European Research Council (ERC) under the European Union's Horizon 2020 Research and Innovation program (Proposal 787527). K. Armstrong provided support with measurements at the Advanced Light Source 12.2.2. The Advanced Light Source is supported by the Director, Office of Science, Office of Basic Energy Sciences, of the U.S. Department of Energy under Contract No. DE-AC02-05CH11231. Beamline 12.2.2 is partially supported by COMPRES, the Consortium for Materials Properties Research in Earth Sciences under NSF Cooperative Agreement EAR 1606856.

Author contributions

W.P.H. conceived, designed, and supervised the project. W.P.H., Y.C.T., A.P., and S.M.D. conducted experiments and analyzed data. H.B. provided the samples. F.W. performed supplementary sample analysis. W.P.H. and F.D. wrote the original manuscript. All authors reviewed and commented on the final version of the manuscript.

Competing interests

The authors declare no competing interests.

Additional information

Supplementary information The online version contains supplementary material available at https://doi.org/10.1038/s41467-025-65430-7.

Correspondence and requests for materials should be addressed to Wen-Pin Hsieh.

Peer review information *Nature Communications* thanks Youjun Zhang, and the other, anonymous, reviewer(s) for their contribution to the peer review of this work. A peer review file is available.